optica

Strongly asymmetric wavelength dependence of optical gain in nanocavity-based Raman silicon lasers: supplementary material

DAIKI YAMASHITA,[1,*] TAKASHI ASANO,[2] SUSUMU NODA,[2,3] AND YASUSHI TAKAHASHI,[1]

[1]Department of Physics and Electronics, Osaka Prefecture University, Sakai, Osaka 599-8531, Japan
[2]Department of Electronic Science and Engineering, Kyoto University, Kyoto 615-8510 Japan
[3]Photonics and Electronics Science and Engineering Center, Kyoto University, Kyoto 615-8510 Japan
*Corresponding author: d-yamashita@pe.osakafu-u.ac.jp

Published 9 October 2018

This document provides supplementary information to "Strongly asymmetric wavelength dependence of optical gain in nanocavity-based Raman silicon lasers," https://doi.org/10.1364/OPTICA.5.001256.

S1. Raman scattering spectra

Figure S1 shows the Raman scattering spectra that were obtained under excitation of the pump nanocavity mode [Fig. 1(e)]. The spectra were resolved by a monochromator with a focal length of 500 mm and detected by a liquid-nitrogen-cooled InGaAs array. The incident laser was not chopped for this measurement. Each Raman scattering spectrum was measured by adjusting the excitation wavelength (λ_{in}) to the optimum value that maximizes the Stokes emission intensity. This data was taken several months after the measurements of the stimulated-Raman-scattering excitation (SRE) spectra. The details of the experimental method are provided in previous publications [1,2].

It is noted that the Raman scattered light is emitted through the Stokes nanocavity mode even at excitation powers significantly below the threshold P_{th} (the broad background by the spontaneous Raman scattering is hardly visible since it is very small). Therefore, the linewidth of the emission was approximately 1 pm. The resolution limit of the monochromator is about 100 pm

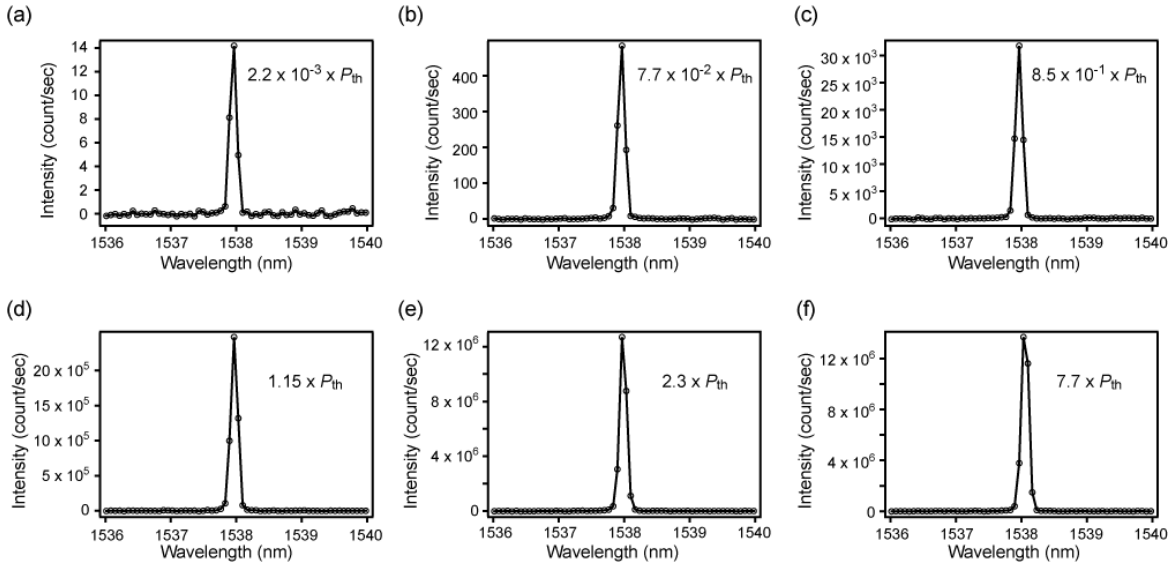

Fig. S1. Raman scattering spectra for various excitation powers. (a) 2.2×10^{-3} P_{th}. (b) 7.7×10^{-2} P_{th}. (c) 8.5×10^{-1} P_{th}. (d) 1.15 P_{th}. (e) 2.3 P_{th}. (f) 7.7 P_{th}. The vertical axis represents the intensity detected by the liquid-nitrogen-cooled InGaAs array.

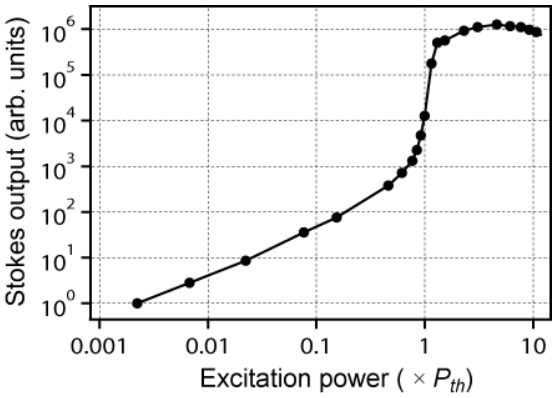

Fig. S2. Laser output power as a function of P_{input}.

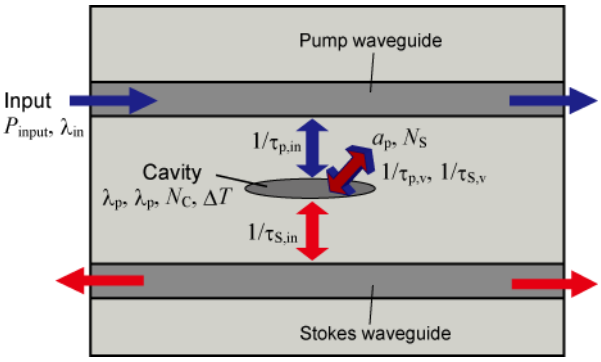

Fig. S3. Schematic of the calculation model.

and thus we were not able to detect the expected linewidth narrowing during lasing. By increasing the input power P_{input}, the peak gradually redshifted mainly due to the adjustment of the λ_{in}.

Figure S2 shows the Raman emission intensity as a function of P_{input}. The intensities were normalized by the intensity at $P_{input} = 2.2 \times 10^{-3}\ P_{th}$. The Raman output power increased linearly in the low pump-power regime. As P_{input} increased further, the Raman output power started to change nonlinearly and rapidly increased by more than two-orders of magnitude around $P_{input} = P_{th}$.

S2. Calculated results using coupled mode theory

Here, we describe the calculation method and the original numerical data used to draw the spectra shown in Fig. 4. We employed a calculation framework based on coupled mode theory [3–5]. Figure S3 shows an overview of the calculation model. We used the following cavity parameters: $Q_P = 170{,}000$, $Q_S = 1{,}600{,}000$, and $\Delta f = 15.614$ THz. Although these values are slightly different from those of the samples measured in the main text, no significant differences appeared in the calculation results. The details of the other parameters are explained in our previous paper [5].

The time evolution of the number of photons confined in the two nanocavity modes can be calculated with the rate equations for the amplitude of the pump light (a_p) [3],

$$\frac{da_p}{dt} = \left(-\frac{1}{2\tau_{p,total}} + i\omega_p'\right)a_p - g_R^{cav}\left(N_S+1\right)a_p + \sqrt{\frac{P_{input}}{2\tau_{p,in}}}e^{i\omega_{in}t}, \quad \text{(S1)}$$

and the number of photons in the Stokes mode (N_S) [4],

$$\frac{dN_S}{dt} = -\frac{N_S}{\tau_{S,total}} + 2g_{R,detuning}^{cav}\left(N_S+1\right)N_p. \quad \text{(S2)}$$

The amplitude and the photon number are related via $N_i = |a_i|^2/\hbar\omega_i$ where either p or S can be substituted for the index i to represent the equations for the pump and Stokes mode, respectively. $\tau_{i,total}$ (i = p, S) is defined as the photon lifetime of the cavity mode including the photon leakage from the cavity and the losses due to TPA [see Eq. (S7)]. ω_i' is the angular frequency of the resonance peak, which shifts as a function of time due to three nonlinear effects: the carrier-plasma effect, the thermo-optic effect and the Kerr effect. Therefore, ω_i' can be written as

$$\omega_i'(t) = \omega_i - \frac{\Delta n_{i,carrier}}{n_i}\omega_i - \frac{\Delta n_{i,thermal}}{n_i}\omega_i - \frac{\Delta n_{i,Kerr}}{n_i}\omega_i. \quad \text{(S3)}$$

The refractive index of silicon (Si) for the pump mode and Stokes mode is n_i (i = p, S). $\Delta n_{i,carrier}$ [see Eqs. (S16) and (S17)], $\Delta n_{i,thermal}$ [see Eq. (S18)] and $\Delta n_{i,Kerr}$ are the individual contributions to the total shift of the refractive index due to the carrier-plasma effect, the thermo-optic effect and the Kerr effect, respectively. It has been demonstrated that $\Delta n_{i,Kerr}$ is much smaller than the other contributions [5]. g_R^{cav} is the Raman gain coefficient of the nanocavity [see Eq. (S13)] and $g_{R,detuning}^{cav}$ is the Raman gain coefficient that accounts for the detuning between the peak of the spontaneous Raman scattering and the resonance peak of the Stokes mode [see Eq. (S15)]. Further, $1/\tau_{p,in}$ is the coupling strength between the propagating light in the pump excitation waveguide and the pump nanocavity mode as shown in Fig. S3. Finally, P_{input} is the power of the excitation light in the pump waveguide, and $\omega_{in} = 2\pi c/\lambda_{in}$.

The temporal evolution of the free-carrier density in the nanocavity, N_C, is given by the following rate equation.

$$\frac{dN_C}{dt} = -\frac{N_C}{\tau_{carrier}} + G_{carrier}. \quad \text{(S4)}$$

Here, $\tau_{carrier}$ is the dissipation time of the free carriers in the nanocavity, determined by nonradiative recombination and carrier diffusion. $G_{carrier}$ is the generation rate of free carriers, *i.e.*, the carriers generated by the TPA process [see Eq. (S19)].

The energy of the light absorbed by TPA and FCA is ultimately converted into heat through three different processes [see Eqs. (S20)–(S23)] and this induces a temperature rise of the cavity material. In order to properly evaluate the temperature change of the nanocavity, we considered that the heat generated in the cavity diffuses to the surrounding photonic crystal (PC). The changes in cavity temperature and surrounding temperature are denoted as ΔT_{cav} and $\Delta T_{surround}$, respectively. They were evaluated using

$$\frac{d\Delta T_{cav}}{dt} = -\frac{\Delta T_{cav} - \Delta T_{surround}}{\tau_{heat,cav}} + G_{heat}, \quad \text{(S5)}$$

and

$$\frac{d\Delta T_{surround}}{dt} = -\frac{\Delta T_{surround}}{\tau_{heat,surround}} + \frac{C_v^{cav}}{C_v^{surround}}\frac{\Delta T_{cav} - \Delta T_{surround}}{\tau_{heat,cav}}, \quad \text{(S6)}$$

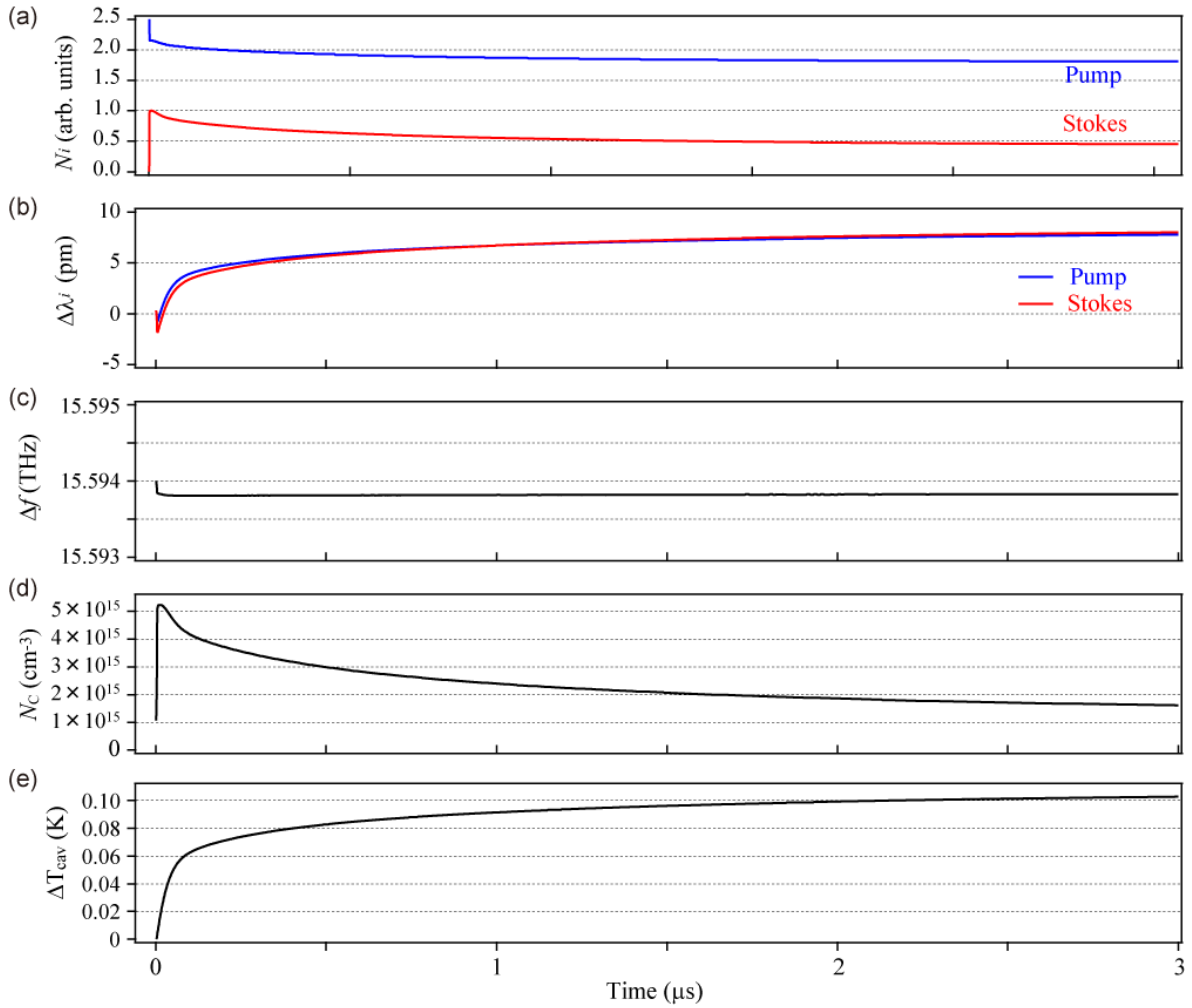

Fig.S4. Time evolution of characteristic properties in a Raman Si nanocavity laser for 8.0 × P_{th} and $\lambda_{in} = \lambda_{p,0}$. The open circles in Fig. 4 correspond to these calculation results. (a) Calculated time evolution of the number of photons in the pump mode (blue) and the Stokes mode (red). The curves are normalized by the peak value of N_S at 10 ns. (b) Relative shifts of the resonance peak wavelengths for the pump mode (blue) and Stokes mode (red). (c) Frequency spacing between the pump mode and the Stokes mode. (d) Carrier density generated by TPA. (e) Temperature change of the cavity.

where G_{heat} [see Eq. (S20)] and $1/\tau_{heat,cav}$ are the heat generation rate and the temperature decay rate of the cavity, respectively. Equation (S6) shows that the surrounding PC is connected to the thermal reservoir (environment) and approaches the thermal equilibrium according to the time constant $\tau_{heat,surround}$. C_v^{cav} and $C_v^{surround}$ are the heat capacities of the cavity and the surrounding PC, respectively.

Figure S4 shows the calculation results for an excitation power of 8.0 × P_{th} and an excitation wavelength of $\lambda_{in} = \lambda_{p,0}$. The origin of the horizontal time axis indicates the start of the excitation. The blue and red curves in Fig. S4(a) show the normalized time evolutions of the number of photons in the pump mode, $N_p = |a_p|^2/\hbar\omega_p$, and the Stokes mode, N_S, respectively. Depending on λ_{in}, P_{input}, and the thermal reservoir, an oscillating behavior may be observed during Raman lasing [5], but in the present condition no oscillation appears. Figure S4(b) shows the relative shifts of the resonance peak wavelengths for the pump nanocavity mode ($\Delta\lambda_p$) and for the Stokes mode ($\Delta\lambda_S$) with respect to the corresponding intrinsic values. Initially, a blueshift of the resonance peak positions is observed due to the plasma effect, but then the resonance peaks gradually redshift due to the increase of the cavity temperature, which is shown in Fig. S4(e). Figure S4(c) shows the frequency spacing between the two nanocavity modes, Δf. As shown in Fig. S4(b), the magnitudes of $\Delta\lambda_p$ and $\Delta\lambda_S$ are similar. Therefore, the induced shift Δf is very small. Figure S4(d) shows the carrier density that is generated by TPA, N_C. The carrier density N_C rapidly increases within a short time after the start of the excitation, but for later times it gradually decreases because of the detuning between the λ_{in} and λ_p [the latter changes as shown in Fig. S4(b)]. Figure S4(e) presents the temperature change of the cavity, ΔT_{cav}.

The calculation predicts that the emission converges to a stable level within several μs after start of the excitation. The spectral data in Fig. 4 were obtained from the converged values.

S3. SRE spectra without modulation of the pump laser

As shown in Fig. 2 in the main text, we modulated the pump laser light by placing a mechanical chopper in the excitation path. Such a setup allows us to avoid the hysteresis response of the SRE spectrum that is observed by changing the λ_{in} sweeping direction. The hysteresis occurs due to the accumulation of heat generated by the TPA carriers. However, by chopping the excitation beam

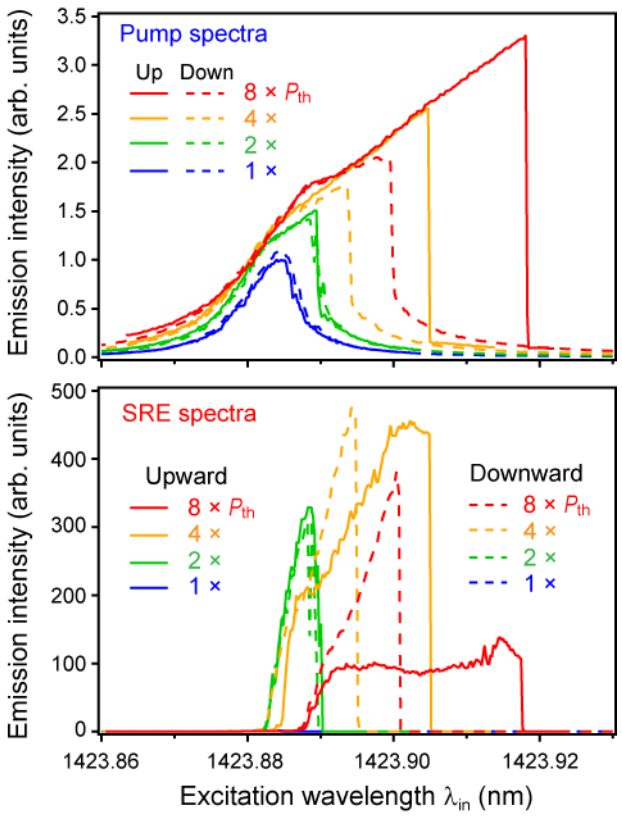

Fig. S5. Resonance spectra for the pump mode (upper panel) and SRE spectra (lower panel) in case of continous laser illumination. The solid lines show the spectra for the upward sweeping direction of λ_{in} while the dashed lines are that for the downward scan. The spectra are normalized by the peak intensity observed for $1.0 \times P_{th}$.

(which has a wavelength λ_{in} that is redshifted with respect to $\lambda_{p,0}$), the cavity resonance wavelength changes periodically between the cold-equilibrium wavelength $\lambda_{p,0}$ (beam blocked) to the warm-equilibrium wavelength (beam open), while passing through a non-equilibrium state. It is well known that the emissions from high-Q microcavities often oscillate in such a non-equilibrium state [5–7]. However, it has been demonstrated that the Raman laser signal converges to a stable operation condition within a few microseconds of continuous laser excitation [5]. Accordingly, the results shown in Figs. 3 and 5 should reflect the shape of the gain in actual devices.

On the other hand, for the application of Raman lasers, the responses without pump modulation can also be useful. Figure S5 presents the resonance spectra of the pump mode (upper panel) and the corresponding SRE spectra (lower panel) that were observed when the mechanical chopper is placed in the collection path just before the photodiode in Fig. 2. Although an hysteresis response was clearly observed for high excitation ($4.0 \times P_{th}$ and $8.0 \times P_{th}$), the spectral shapes of the SRE data for the upward sweeping direction were similar to those shown in Fig. 3(b). These results suggest that optical bistable switching with a switching contrast larger than 30dB can be obtained using the nanocavity-based Raman Si laser [8].

Finally, we comment on the reproducibility of the results. We confirmed that the setup shown in Fig. 2 reproduces the SRE spectra shown in Fig. 3 with good accuracy. In addition, similar results were obtained even for samples with different Q and Δf. On the other hand, the reproducibility is not high when the pump laser is not modulated, probably due to the strong thermo-optic effect. Here, the spectral shapes for the upward and downward scans for $4.0 \times P_{th}$ and $8.0 \times P_{th}$ were different in each measurement. Fluctuations in the heat diffusion from the cavity to the surrounding PC, the high-Q_S value, and the carrier lifetime due to the occupation of surface states may be responsible for this complex behavior. These effects will be important issues for improving the laser performance. The differences between the two measurements suggests that the temperature drift of the nanocavity does not completely stop even within 0.5 milliseconds of continuous laser excitation with high excitation powers.

Appendix

Below we present the equations employed to derive the calculation results presented in Section S2.

The $1/\tau_{i,\mathrm{total}}$ (i = p, S) in Eqs. (S1) and (S2) is the rate of the energy loss in the cavity. It has several contributions as shown in Eq. (S7).

$$1/\tau_{i,total} = 1/\tau_{i,in} + 1/\tau_{i,v} + 1/\tau_{i,TPA} + 1/\tau_{i,FCA}. \quad \text{(S7)}$$

Here, $1/\tau_{i,\mathrm{in}}$ and $1/\tau_{i,\mathrm{v}}$ represent the rates of energy transfer into the waveguide (in-plane direction) and into free space (vertical direction), respectively. $1/\tau_{i,\mathrm{TPA}}$ is defined as the loss rate due to TPA (proportional to the energy stored in the cavity). $1/\tau_{i,\mathrm{FCA}}$ is defined as the loss rate due to FCA (proportional to the carrier density, N_C) and is calculated via $1/\tau_{i,\mathrm{FCA}} = \omega/Q_{i,\mathrm{FCA}}$. Q_S is determined from the relationship $1/Q_S = 1/Q_{S,\mathrm{in}} + 1/Q_{S,\mathrm{v}} + 1/Q_{S,\mathrm{TPA}} + 1/Q_{S,\mathrm{FCA}}$ at strong excitation conditions.

$1/\tau_{i,\mathrm{TPA}}$, (i = p, S) can be written as [3]

$$\frac{1}{\tau_{\mathrm{p,TPA}}} = \frac{\beta_{\mathrm{Si}} c^2}{n_{\mathrm{p}}^2 V_{\mathrm{p,TPA}}} |a_p|^2 + \frac{\beta_{\mathrm{Si}} c^2}{n_{\mathrm{p}}^2 V_{o,\mathrm{TPA}}} 2|a_{\mathrm{S}}|^2, \quad \text{(S8)}$$

and

$$\frac{1}{\tau_{\mathrm{S,TPA}}} = \frac{\beta_{\mathrm{Si}} c^2}{n_{\mathrm{S}}^2 V_{\mathrm{S,TPA}}} |a_{\mathrm{S}}|^2 + \frac{\beta_{\mathrm{Si}} c^2}{n_{\mathrm{S}}^2 V_{o,\mathrm{TPA}}} 2|a_{\mathrm{p}}|^2, \quad \text{(S9)}$$

where the first terms represent the TPA process involving either two pump photons or two Stokes photons. The second terms represent the simulataneous absorption process involving one pump photon and one Stokes photon. β_{Si} denotes the TPA coefficient of bulk silicon. The effective mode volume for TPA, $V_{i,\mathrm{TPA}}$, is [3]

$$V_{i,\mathrm{TPA}} = \frac{\left(\int n_i^2(r)|E_i(r)|^2 dr^3\right)^2}{\int_{\mathrm{Si}} n_i^4(r)|E_i(r)|^4 dr^3}. \quad \text{(S10)}$$

$V_{o,\mathrm{TPA}}$ describes the spatial overlap between the pump mode and the Stokes mode, and we consider $V_{o,\mathrm{TPA}} = V_R$. The latter is provided in Eq. (S14).

Then we have

$$\frac{1}{\tau_{i,FCA}} = \frac{c}{n_i}(\sigma_{i,e} + \sigma_{i,h}) N_{\mathrm{C}}. \quad \text{(S11)}$$

with c being the speed of light in vacuum. The absorption cross-sections for electrons and holes, $\sigma_{i,e}$ and $\sigma_{i,h}$, can be written as

$$\sigma_{i,e/h} = \frac{e^2}{c n_i \omega_i^2 \varepsilon_0 m_{e/h}^* \tau_{relax,e/h}}, \quad \text{(S12)}$$

where e is the electron charge, ε_0 is the vacuum permittivity, m_e^* and m_h^* are the effective masses of the electron and hole, respectively, and $\tau_{relax,e/h}$ is the corresponding relaxation time.

g_R^{cav} in Eq. (S1) is defined as [4]

$$g_R^{\mathrm{cav}} = \left(\frac{\hbar \omega_{\mathrm{in}} c^2}{2 n_{\mathrm{p}} n_{\mathrm{S}} V_R} \right) g_R^{\mathrm{bulk}}, \tag{S13}$$

where g_R^{bulk} denotes the Raman gain coefficient of bulk Si. V_R is the effective modal volume for Raman scattering, which determines the spatial overlap between the pump and Stokes modes. It can be calculated using the following expression.

$$V_R = \frac{\int \varepsilon_{\mathrm{p}} E_{\mathrm{p}}^2 dV \int \varepsilon_{\mathrm{S}} E_{\mathrm{S}}^2 dV}{\varepsilon_{\mathrm{p}} \varepsilon_{\mathrm{S}} \sum_{ijkl} \int_{\mathrm{Si}} \chi_{ijkl}^R E_{\mathrm{p},i} E_{\mathrm{S},j}^* E_{\mathrm{S},k} E_{\mathrm{p},l}^* dV}. \tag{S14}$$

Here, ε_i is the dielectric constant in Si and E_i is the electric field. χ_{ijkl}^R is the fourth-order tensor corresponding to the Raman effect in Si. We note that V_R depends on both the crystal orientation and the overlap between the electric fields of the pump and Stokes modes. By choosing the crystal direction [100] for the nanocavity-based Raman Si laser we were able to maximize the Raman emission and realized optimum lasing operation.

$g_{R,\mathrm{detuning}}^{\mathrm{cav}}$ in Eq. (S2) is defined in the following Eq. (S15).

$$g_{R,\mathrm{detuning}}^{\mathrm{cav}} = g_R^{\mathrm{cav}} \frac{\left(\frac{\Delta}{2} \right)^2}{\left(\omega_{\mathrm{S}}' + \Delta f_R - \omega_{\mathrm{in}} \right)^2 + \left(\frac{\Delta}{2} \right)^2}. \tag{S15}$$

The Δ is the full width at half-maximum of the spontaneous Raman scattering in Si and Δf_R is the Raman shift of the Si nanocavity.

The partial shifts of the refractive index induced by the carrier-plasma effect and the thermo-optic effect in Eq. (S3) are defined as [3]

$$\Delta n_{\mathrm{p,carrier}} = \frac{e^2 N_{\mathrm{C}}}{2 \varepsilon_0 n_{\mathrm{p}} \omega_{\mathrm{in}}^2} \left(\frac{1}{m_e^*} + \frac{1}{m_h^*} \right), \tag{S16}$$

$$\Delta n_{\mathrm{S,carrier}} = \frac{e^2 N_{\mathrm{C}}}{2 \varepsilon_0 n_{\mathrm{S}} \omega_{\mathrm{S}}^2} \left(\frac{1}{m_e^*} + \frac{1}{m_h^*} \right), \tag{S17}$$

$$\Delta n_{i,\mathrm{thermal}} = \frac{dn_i}{dt} \Delta T, \tag{S18}$$

The generation rate of the free carriers G_{carrier} in Eq. (S4) can be calculated from the mode-averaged TPA loss rate [4],

$$\begin{aligned} G_{\mathrm{carrier}} = & \frac{\beta_{\mathrm{Si}} c^2}{2 \hbar \omega_{\mathrm{in}} n_{\mathrm{p}}^2 V_{\mathrm{p,FCA}}^2} |a_{\mathrm{p}}|^4 + \frac{\beta_{\mathrm{Si}} c^2}{2 \hbar \omega_{\mathrm{S}}' n_{\mathrm{S}}^2 V_{\mathrm{S,FCA}}^2} |a_{\mathrm{S}}|^4 \\ & + \frac{\beta_{\mathrm{Si}} c^2}{\hbar (\omega_{\mathrm{in}} + \omega_{\mathrm{S}}') n_{\mathrm{p}}^2 V_{\mathrm{o,FCA}}^2} 2 |a_{\mathrm{S}}|^2 |a_{\mathrm{p}}|^2 \\ & + \frac{\beta_{\mathrm{Si}} c^2}{\hbar (\omega_{\mathrm{in}} + \omega_{\mathrm{S}}') n_{\mathrm{S}}^2 V_{\mathrm{o,FCA}}^2} 2 |a_{\mathrm{p}}|^2 |a_{\mathrm{S}}|^2 \end{aligned}. \tag{S19}$$

The effective mode volume for FCA is obtained from $V_{\mathrm{FCA}}^2 = V_{\mathrm{TPA}} \times V_{\mathrm{carrier}}^{\mathrm{cav}}$. $V_{\mathrm{carrier}}^{\mathrm{cav}}$ is the cavity volume for the free carriers and is defined as the product (cavity length) · (distance between the air holes nearest to the center of the cavity in the y direction) · (slab thickness) [9].

The heat generation rate G_{heat} in Eq. (S5) is expressed as a sum of three terms:

$$G_{\mathrm{heat}} = G_{\mathrm{heat,TPA\text{-}relax}} + G_{\mathrm{heat,FCA\text{-}relax}} + G_{\mathrm{heat,recomb}}. \tag{S20}$$

$G_{\mathrm{heat,TPA\_relax}}$ denotes the heat generation rate due to relaxation of TPA carriers to the bottom of the conduction band, $G_{\mathrm{heat,FCA\_relax}}$ is the heat generation rate due to relaxation of carriers generated by FCA, and the heat generation rate for nonradiative interband recombination of the carriers is represented as $G_{\mathrm{heat,recomb}}$. These rates are calculated using the following three equations.

$$\begin{aligned} G_{\mathrm{heat,TPA\text{-}relax}} = & \frac{|a_{\mathrm{p}}|^2}{\tau_{\mathrm{p,TPA}}} \times \frac{2 \hbar \omega_{\mathrm{in}} - E_g}{2 \hbar \omega_{\mathrm{in}}} \times \frac{1}{C_v^{\mathrm{cav}}} \\ & + \frac{|a_{\mathrm{S}}|^2}{\tau_{\mathrm{S,TPA}}} \times \frac{2 \hbar \omega_{\mathrm{S}} - E_g}{2 \hbar \omega_{\mathrm{S}}} \times \frac{1}{C_v^{\mathrm{cav}}} \end{aligned} \tag{S21}$$

$$G_{\mathrm{heat,FCA\text{-}relax}} = \frac{|a_{\mathrm{p}}|^2}{\tau_{\mathrm{p,FCA}}} \times \frac{1}{C_v^{\mathrm{cav}}} + \frac{|a_{\mathrm{S}}|^2}{\tau_{\mathrm{S,FCA}}} \times \frac{1}{C_v^{\mathrm{cav}}} \tag{S22}$$

$$G_{\mathrm{heat,recomb}} = \frac{N V_{\mathrm{carrier}}^{\mathrm{cav}}}{\tau_{\mathrm{carrier}}} \times E_g \times \frac{1}{C_v^{\mathrm{cav}}} \tag{S23}$$

Finally, E_g is the bandgap energy of Si. To simplify the calculations, we assume that all carriers generated by TPA recombine in the surrounding PC region.

References

1. Y. Takahashi, Y. Inui, M. Chihara, T. Asano, R. Terawaki, and S. Noda, "A micrometre-scale Raman silicon laser with a microwatt threshold," Nature **498**, 470-474 (2013).
2. D. Yamashita, Y. Takahashi, T. Asano, and S. Noda, "Raman shift and strain effect in high-*Q* photonic crystal silicon nanocavity," Opt. Express **23**, 3951-3959 (2015).
3. X. Yang and C. Wong, "Coupled-mode theory for stimulated Raman scattering in high-Q/V_m silicon photonic band gap defect cavity lasers," Opt. Express **15**, 4763 (2007).
4. X. Checoury, Z. Han, and P. Boucaud, "Stimulated Raman scattering in silicon photonic crystal waveguides under continuous excitation," Phys. Rev. B **82**, 041308(R) (2010).
5. D. Yamashita, T. Asano, S. Noda, and Y. Takahashi, "Lasing dynamics of optically-pumped ultralow-threshold Raman silicon nanocavity lasers", Phys. Rev. Applied **10**, 024039 (2018).
6. T. Carmon, L. Yang, and K. J. Vahala, "Dynamical thermal behavior and thermal selfstability of microcavities," Opt. Express **12**, 4742–4750 (2004).
7. J. Yang, T. Gu, J. Zheng, M. Yu, G.-Q. Lo, D.-L. Kwong, and C. W. Wong, "Radio frequency regenerative oscillations in monolithic high-Q/V heterostructured photonic crystal cavities," Appl. Phys. Lett. **104**, 061104 (2014).
8. M. Notomi, A. Shinya, S. Mitsugi, G. Kira, E. Kuramochi, and T. Tanabe, "Optical bistable switching action of Si high-Q photonic-crystal nanocavities," Opt. Express **13**, 2678-2687 (2005).
9. T. Uesugi, B. S. Song, T. Asano, and S. Noda, "Investigation of optical nonlinearities in an ultra-high-Q Si nanocavity in a two-dimensional photonic crystal slab," Opt. Express **14**, 377 (2006).